J. Marine Sci. Appl. (2015) 14: 302-315
DOI: 10.1007/s11804-015-1322-x

Dynamic Adaptive Finite Element Analysis of Acoustic Wave Propagation Due to Underwater Explosion for Fluid-structure Interaction Problems

Seyed Shahab Emamzadeh[1*], Mohammad Taghi Ahmadi[2], Soheil Mohammadi[3] and Masoud Biglarkhani[4]

1. Islamic Azad University, Kangan Branch, Kangan 7557146845, Iran
2. Department of Civil Engineering, Tarbiat Modares University, Tehran 14115-143, Iran
3. School of Civil Engineering, University of Tehran, Tehran 4563-11155, Iran
4. Department of Civil Engineering, University of Hormozgan, Hormozgan 3995, Iran

Abstract: In this paper, an investigation into the propagation of far field explosion waves in water and their effects on nearby structures are carried out. For the far field structure, the motion of the fluid surrounding the structure may be assumed small, allowing linearization of the governing fluid equations. A complete analysis of the problem must involve simultaneous solution of the dynamic response of the structure and the propagation of explosion wave in the surrounding fluid. In this study, a dynamic adaptive finite element procedure is proposed. Its application to the solution of a 2D fluid-structure interaction is investigated in the time domain. The research includes: a) calculation of the far-field scatter wave due to underwater explosion including solution of the time-depended acoustic wave equation, b) fluid-structure interaction analysis using coupled Euler-Lagrangian approach, and c) adaptive finite element procedures employing error estimates, and re-meshing. The temporal mesh adaptation is achieved by local regeneration of the grid using a time-dependent error indicator based on curvature of pressure function. As a result, the overall response is better predicted by a moving mesh than an equivalent uniform mesh. In addition, the cost of computation for large problems is reduced while the accuracy is improved.

Keywords: adaptive mesh; fluid-structure interaction; acoustic wave; finite element analysis; underwater explosion

Article ID: 1671-9433(2015)03-0302-14

1 Introduction

Most problems of dynamic fluid-structure interaction (FSI) in acoustic media around hydraulics and marine structures are solved by the finite element method (FEM). For example, dynamical response of a concrete dam subjected to underwater contact explosion has numerically investigated by Yu (2009) or ship shock modeling under far-field underwater explosion by Shin (2004). Although experimental works have down in this field such as Ghanaat *et al*. (1992). In his work, an experimental study of dam-water-foundation interaction has down on a full scale dam in China. However, even after more than 40 years of development of FEM, the question of estimating and controlling the discretization errors has remained as a major challenge. Several FEM modifications have been reported for improving the results. Sprague and Geers (2008) have developed a Legendre spectral finite elements algorithm for structural dynamics analysis. Ross *et al*. (2008; 2009) proposed the localized Lagrange multiplier method for acoustic FSI. In these coupled Euler-Lagrange works, fixed uniform meshes are considered for the whole analyses. As fine meshes are required where large gradients exist in the solution, such computations are not optimum. Other methods such as arbitrary Lagrangian-Eulerian (ALE) ones have been reviewed by Mair (1999). Kim and Shin (2008) have recently applied ALE techniques to underwater explosion analysis of a submarine liquefied oxygen tank. Lagrangian motion was computed at every time step, followed by a re-map phase in which the spatial mesh was alternatively not re-zoned (as Lagrangian), re-zoned to its original shape (as Eulerian) or re-zoned to some more "advantageous" shape (as somehow between Lagrangian and Eulerian). ALE technique is usually employed to preserve a uniform mesh and not used to enhance the physical phenomena itself. Thus, its spatial description of the mesh is neither restricted to follow the material motions (as in Lagrangian) nor does it remain as fixed in space (as in Eulerian). One of the main concerns in acoustic finite element analysis is the adequacy of the finite element mesh to solve the dilatational wave equation that governs the fluid behavior. The Galerkin method provides good accuracy as long as the mesh is fine enough to comply with the maximum wave number. This is a criterion often too expensive even for moderate wave numbers. Moreover, a non-uniform finite element mesh is needed in many practical problems because increasingly finer grids are required near singularities and non-smooth boundaries. Nevertheless, such a discretization process is still unable to provide a proper resolution and order of the approximation at the required locations despite quite fine meshes. An h-adaptive finite

Received date: 2014-10-22.
Accepted date: 2015-02-27.
***Corresponding author Email:** Emamzadeh1393@kanganiau.ac.ir

element strategy for acoustic problems was presented by Bausys and Wiberg (1999), among the others. Their method's key features are error estimation, adaptive mesh generation and re-meshing for finite element analysis using the superconvergent patch recovery technique for prime variables. In this process a highly reliable estimation of the discretization errors is crucial. Bouillard *et al*. (1996) implemented the original superconvergent patch recovery (SPR) technique for acoustic finite element analysis. They extended the original concept to complex variables and studied the reliability of the error estimation process.

Tetambe and Rajakumar (1996) presented the error estimation strategy for acoustic analysis based on nodal averaging technique. A residual-based a posteriori error estimator for Helmholtz equation was presented by Harari *et al*. (1996). Recently, many efforts have been made for dynamic adaptive finite elements. Kadioglu and Sussman (2008) presented adaptive solution techniques for simulating underwater explosions and implosions. They solved several test problems to show the performance of their methods and validated the results by comparing shock speed, shock amplitude, and material interface speed, with benchmark results produced by Wardlaw (1998). Finally, their effort indicated that for some specific cases, e.g. investigating bubble growth and collapse dynamics, that the semi-implicit approach is significantly more efficient than an explicit approach.

Early, in order to solving hyperbolic conservation laws adaptive mesh refinement techniques are developed (Bell *et al*., 1994). These extended to solve the compressible Navier–Stokes equations accordingly Skamarock and Klemp (1993) and Steinthorsson *et al*. (1995). The significant efforts have been performed by them in order to solve incompressible or weakly compressible flows adaptively by Stevens and Bretherton (1996), Howell and Bell (1997) and Pember *et al*. (1998).

Recently, an adaptive method is developed for solving one-dimensional systems of hyperbolic conservation laws, which combines the rezoning approach with the finite volume weighted essentially non-oscillatory scheme (Hua *et al*., 2015). They found this adaptive method exhibits more accurate resolution of discontinuities for a similar level of computational time comparing with that on a uniform mesh.

Dapogny *et al*. (2014) propose a method for dealing with the problem of mesh deformation (or mesh evolution) in the context of free and moving boundary problems, in three space dimensions. Their method would have been considered in the fields of mesh generation, shape optimization, and computational fluid dynamics.

Berrone and Marro (2009) presented space–time adaptive simulations for unsteady Navier–Stokes problems. The fluid domain was discretized by structured triangular finite element mesh and the unsteady flow was traced with a posteriori estimates and adaptive algorithms.

In the present research an adaptive FE strategy has used that employ refined mesh only in wave front and provide reduced equations. This refining has also been a terminated optimal refining. Early works with traditional FE employ refined mesh in whole domain of analysis. The main difference of the content and advantages of the following is adapting the mesh refining with wave length and wave frequency. Usually in wave front the wave frequency is high and consequently wave length decreases, so a refining mesh has developed for optimal covering of wave front length.

In the present study, the error estimation has been performed using curvature based error indicators for prime variables of finite element approximation. For mesh generation and re-meshing, the program MESH2D is adopted employing the advancing front technique. This program was originally prepared by Gilardo (1995) for compressible flow. The finite element code ZFEAP, prepared by Emamzadeh (2008), is used for adaptive fluid-structure interaction problem. Numerical examples are shown to illustrate the efficiency of the proposed error indicator and adaptive strategy procedure.

2 Underwater explosion and pressure wave distribution

The pressure load acting on a structure due to an underwater explosion (UNDEX) changes with respect to both time and space. The pressure time history at the standoff point (the point where the wave hits the structure first) is given. The incident pressure p_I at a point j with vector coordinate x_j can be written as:

$$P_I(x_j,t) = P_t(t)P_x(x_j) \tag{1}$$

where $P_t(t)$ is the pressure time history at the standoff point x_0, and $P_x(x_j)$ is the spatial function, at an arbitrary point x_j. For a plane wave:

$$P_x(x_j) = 1 \tag{2}$$

By considering the time delay required for the wave to travel from the standoff point to an arbitrary point, it is found that

$$p_I(x_j,t) = p_t\left(t - \frac{R_j - R_0}{c_f}\right)p_x(x_j) = p_t(\tau_j)p_x(x_j) \tag{3}$$

where

$$R_j = \frac{\left|(x_j - x_s)\cdot(x_o - x_s)\right|}{x_s - x_o} \tag{4}$$

where x_s is considered to be the specified source point of explosion. c_f is the wave velocity in the fluid and τ_j known as the "retarded time" corresponds to the time lag for the pressure wave to travel from the standoff point. Detailed basic formulation of the incident wave can be found in Cole (1948).

3 Modeling of fluid-structure interaction phenomenon by CEL approach

If a continuum deforms or flows, the position of the small

volumetric elements changes with time. These positions can be described as functions of time in two ways. Lagrangian describes it as the movement of the continuum is specified as a function of its initial coordinates and time. Eulerian describes it as the movement of the continuum is specified as a function of its instantaneous position and time. In simulations with Lagrangian formulation the interface between two parts is precisely defined and tracked. In these simulations large deformation of a part leads to hopeless mesh and element distortion. In Eulerian analysis an Eulerian reference mesh, which remains undistorted and does not move is needed to trace the motion of the particles. The advantage of an Eulerian formulation is that no element distortions will occur. Disadvantageously, the interface between two parts cannot be described as precise as if a Lagrangian formulation is used. The ALE method can be considered a superset of both the Eulerian and Lagrangian method, since both types of mesh motions are incorporated within an ALE Scheme. The ALE method cannot be considered a superset for allowing an Eulerian region to interact with a Lagrangian interface. In the following, Lagrangian approach has been selected for structure and Eulerian approach has been selected for surrounding fluid.

When a structure is exposed to UNDEX, it deforms and displaces the surrounding fluid, by the scattered pressure wave. Thus, the sum of the known incident pressure (as in Eq. (1)) and the unknown scattered pressure are applied to the structure as a result of the fluid-structure interaction. The equilibrium equation for small motions of an acoustic fluid with velocity-dependent losses is taken to be as:

$$\nabla p + \gamma \dot{u}^f + \rho_f \ddot{u}^f = 0 \tag{5}$$

where p is hydrodynamic pressure in excess to hydrostatic pressure. $\dot{u}^f$, $\ddot{u}^f$ are velocity and acceleration vectors of fluid particles, respectively. ρ_f is fluid density and γ is the "volumetric drag" (force per unit volume for unit velocity).

Fluid behavior is assumed to be in viscid, linear, and compressible, so

$$p = -K_f(\nabla \cdot u^f) \tag{6}$$

where K_f and u^f are the bulk modulus and displacement vector of fluid particles, respectively. By dividing Eq. (5) by ρ_f, taking its divergence, neglecting spatial variation of, γ / ρ_f and combining the result with the time derivatives of Eq. (6) one obtains the equation of transient motion for the fluid in terms of the fluid pressure:

$$\frac{1}{K_f}\ddot{p} + \frac{\gamma}{\rho_f K_f}\dot{p} - \frac{1}{\rho_f}\nabla^2 p = 0 \tag{7}$$

An equivalent weak form of Eq. (7) is obtained by introducing an arbitrary variational field, δp , and integrating over the fluid domain V_f

$$\int_{V_f} \delta p \left(\frac{1}{K_f}\ddot{p} + \frac{\gamma}{\rho_f K_f}\dot{p} - \frac{1}{\rho_f}\nabla^2 p \right) \mathrm{d}V = 0 \tag{8}$$

Integration by parts allows this to be rewritten as:

$$\int_{V_f} \left(\delta p \left(\frac{1}{K_f}\ddot{p} + \frac{\gamma}{\rho_f K_f}\dot{p} \right) + \frac{1}{\rho_f}\nabla \delta p \cdot \nabla p \right) \mathrm{d}V + \int_S \delta p \left(\frac{1}{\rho_f} n \cdot \nabla p \right) \mathrm{d}s \tag{9}$$

Assuming that p is prescribed on S_{fp}, the equilibrium equation, Eq. (5), is used on the remainder of the boundary to relate the pressure gradient to the motion of the boundary:

$$n \cdot \left(\frac{1}{\rho_f}\nabla p + \frac{\gamma}{\rho_f}\dot{u}^f + \ddot{u}^f \right) = 0 \quad \text{on } S - S_{fp} \tag{10}$$

where n is the inward unit vector normal to the fluid boundary. Using this equation, the term $n \cdot \nabla p$ is eliminated from Eq. (9) to produce

$$\int_{V_f} \left(\delta p \left(\frac{1}{K_f}\ddot{p} + \frac{\gamma}{\rho_f K_f}\dot{p} \right) + \frac{1}{\rho_f}\nabla \delta p \cdot \nabla p \right) \mathrm{d}V + \int_{S - S_{fp}} \delta p T_n \mathrm{d}s = 0 \tag{11}$$

where, for convenience, the boundary "traction" term is defined as:

$$T_n = -n \cdot \left(\frac{1}{\rho_f}\nabla p \right) = n \cdot \left(\ddot{u}^f + \frac{\gamma}{\rho_f}\dot{u}^f \right) \text{ on } S - S_{fp} \tag{12}$$

In the absence of volumetric drag this boundary traction is equal to the inward acceleration of the particles of the acoustic medium, i.e.;

$$T_n = n \cdot \ddot{u}^f \quad \text{on} \quad S - S_{fp} \tag{13}$$

Many engineering problems dealing with waves involve infinite domains. Usually, the infinite domain is truncated for computational purposes and the wave problem is solved in a finite domain. Non-reflecting boundaries (NRBs) have to be considered, which must allow the waves to leave the truncated domain avoiding spurious reflections that may pollute the solution in the interior of the computational domain of interest.

There are many types of NRBs, which can be classified into two groups, namely, Non-Reflecting Boundary Conditions (NRBCs) and Non-Reflecting Boundary Layers (NRBLs). NRBCs are boundary conditions on the artificial boundary that absorb impinging waves. On the other hand, NRBLs have the property of absorbing waves that are traveling inside the layer.

Finite element simulation of the time-dependent wave propagation in infinite media requires enforcing the transmitting boundary to replace the truncated far-field infinite domain so as to model the effect of the wave radiation

towards infinity.

The well-known Helmholtz equation governing the pressure p:

$$\nabla^2 p = -\frac{1}{c_f}\frac{\partial^2 p}{\partial^2 t} \tag{14}$$

where

$$c_f = \sqrt{\frac{k_f}{\rho_f}} \tag{15}$$

it is considered to denote the speed of sound in the fluid.

If we consider only variations in x (the horizontal direction) we know that the general solution of Eq. (14) can be written as

$$p = F\left(x - c_f t\right) + G\left(x + c_f t\right) \tag{16}$$

where two waves F and G travel in positive and negative directions of x, respectively. The absence of the incoming wave G means that on infinite boundary we have only

$$p = F\left(x - c_f t\right) \tag{17}$$

Thus

$$\frac{\partial p}{\partial n} = \frac{\partial p}{\partial x} = F' \tag{18}$$

$$\frac{\partial p}{\partial t} = c_f F' \tag{19}$$

where F' denotes the derivative of F with respect to $(x-c_f t)$ by eliminating the unknown function F' the Sommerfeld formulation obtained.

In Eulerian approach, the non-reflecting infinite boundary S_{fi}, Sommerfeld equation (Sommerfeld, 1949) has been used as:

$$\frac{\partial p}{\partial n} = -\frac{1}{c_f}\dot{p} \tag{20}$$

For a rigid boundary,

$$\frac{\partial p}{\partial n} = 0 \tag{21}$$

For the structural interface boundary,

$$\frac{\partial p}{\partial n} = -\rho a_n \tag{22}$$

where a_n is considered to be the normal acceleration. Application of the standard Galerkin discretization to the weak form of the governing equations of structure and fluid leads to a classical coupled problem, expressed by two set of second order differential equations as;

$$\boldsymbol{M}\ddot{u} + \boldsymbol{D}\dot{u} + \boldsymbol{K}u = -\boldsymbol{Q}^{\mathrm{T}} p \tag{23}$$

$$\boldsymbol{E}\ddot{p} + \boldsymbol{A}\dot{p} + \boldsymbol{H}p = \rho\boldsymbol{Q}\ddot{u} \tag{24}$$

where $\boldsymbol{M}$, $\boldsymbol{D}$ and $\boldsymbol{K}$ are the structural mass, damping and stiffness matrices. Also $\boldsymbol{E}$, $\boldsymbol{A}$ and $\boldsymbol{H}$ are the fluid equivalent mass, damping and stiffness matrices, respectively. In the above equations pressure is defined as:

$$p = p_I + p_S \tag{25}$$

where p, p_I and p_s correspond to the total, incident and scattered pressure waves respectively. By substituting Eq. (24) in Eq. (25), the fluid equation is obtained in terms of the unknown scattered pressure term, depicted by p hereinafter for brevity. The resulting equation is solved together with Eq. (23) to obtain the response of the structure. The unknown functions are discretized as:

$$p = \boldsymbol{N}_p \tilde{\boldsymbol{p}} \tag{26}$$

$$u = \boldsymbol{N}_u \tilde{\boldsymbol{u}} \tag{27}$$

where $\tilde{\boldsymbol{u}}$ and $\tilde{\boldsymbol{p}}$ are nodal displacement and pressure vectors of structure and fluid fields, respectively. Linear shape function matrices denote by $\boldsymbol{N}_u$ and $\boldsymbol{N}_p$. The structural matrices are defined as:

$$\boldsymbol{M} = \int_V \rho \boldsymbol{N}_u \boldsymbol{N}_u^{\mathrm{T}} \mathrm{d}V \tag{28}$$

$$\boldsymbol{K} = \int_V \nabla \boldsymbol{N}_u \boldsymbol{B} \nabla \boldsymbol{N}_u^{\mathrm{T}} \mathrm{d}V \tag{29}$$

$$\boldsymbol{D} = \alpha \boldsymbol{M} + \beta \boldsymbol{K} \tag{30}$$

$$\boldsymbol{Q} = \int_{S_{fs}} \boldsymbol{N}_u n \cdot \boldsymbol{N}_p \mathrm{d}s \tag{31}$$

where $\boldsymbol{B}$ is the material elasticity matrix of the structure, $\boldsymbol{D}$ is Rayleigh damping matrix, α and β are proportional to significant frequencies of structural response. The coupling matrix $\boldsymbol{Q}$ relates the structural and fluid nodal forces on interacting surfaces. The structure loading is due to an explosion occurring at a source point in the fluid. For fluid domain, similar matrices are defined as:

$$\boldsymbol{E} = \int_{V_f} \frac{1}{K_f} \boldsymbol{N}_p \boldsymbol{N}_p^{\mathrm{T}} \mathrm{d}V \tag{32}$$

$$\boldsymbol{A} = \int_{S_{fi}} \frac{1}{c_f} \boldsymbol{N}_p \boldsymbol{N}_p^{\mathrm{T}} \mathrm{d}s \tag{33}$$

$$\boldsymbol{H} = \int_{V_f} \frac{1}{\rho_f} \nabla \boldsymbol{N}_p (\nabla \boldsymbol{N}_p)^{\mathrm{T}} \mathrm{d}V \tag{34}$$

where the K_f is the bulk modulus of fluid.

For solving the dynamic equations, Newmark implicit method with fixed time increment is applied in a staggered algorithm. In the following problems, a reliable time increment about 0.1 microseconds is adopted for time discreization.

In the staggered algorithm based on the previous scattered pressure at each time step the structural response is calculated from which the new acceleration could in turn be exerted to the fluid domain boundary. This alternative domains calculation is followed iteratively in the same time step until a convergence be achieved.

4 Adaptive finite elements

In structural problems it is generally desirable to obtain a solution in which an energy norm of error is equally distributed within all elements. Such a norm of error can also be extended to viscous flow especially when it is relatively slow and nearly elliptic. However, according to Zienkiewicz *et al*. (2005) the energy norm has little significance at high speeds, a situation we face due to explosion, and thus we revert to other considerations which simply give an error indicator rather than an error estimator. Among the two available procedures such as gradient and curvature, the curvature based refinement will be adopted in this study.

4.1 Curvature based refinement

The error indicator should remain constant in each element. The *h*-refinement process is applied to first-order triangular elements. Fig. 1 determination of error indicators over the elements is carried out by interpolation error approach. If *x*' is the local coordinate inside an element of length hand *p* is a scalar function, the error in *p* is of order O(h^2) (Peraire *et al*., 1987)

$$e = p - p^h = \tilde{c}h^2 \frac{\mathrm{d}^2 p}{\mathrm{d}x'^2} \approx \tilde{c}h^2 \frac{\mathrm{d}^2 p^h}{\mathrm{d}x'^2} \tag{35}$$

where p^h is the finite element solution and $\tilde{c}$ is a constant.

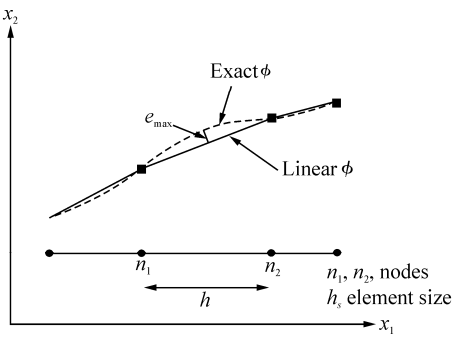

Fig. 1 An element based error defined by Zienkiewicz *et al.* (2005)

If, for instance, it is assumed that $p=p^h$ is at the nodes, i.e. the nodal error is zero, then *e* represents the values on a parabola with a local curvature of $\frac{\mathrm{d}^2 p^h}{\mathrm{d}x'^2}$. The assumption that the nodal values of the function *p* are exact is true only for certain types of interpolating functions and equations. However, according to Zienkiewicz *et al*. (2005), the nodal values remain always more accurate than elsewhere. An element subdivision is sought for equal distribution of errors.

$$h^2 \frac{\mathrm{d}^2 p^h}{\mathrm{d}x'^2} = \bar{C} \tag{36}$$

$\bar{C}$ can be interpreted as a permissible error and so it can be simply insisted that

$$h^2 \frac{\mathrm{d}^2 p^h}{\mathrm{d}x'^2} \le e_p \tag{37}$$

where $e_p = \bar{C}$ is considered to be the user-specified error limit.

If the shape functions of *p* are assumed to be linear, then the second derivatives are difficult to determine. They are difficult to determine because they are clearly zero inside the element and infinity at the element interfaces. Some averaging processes have to be used in order to determine the curvatures from nodal computed values. In two and three dimensional problems, the second derivatives (or curvatures) tensors are given as:

$$\frac{\partial^2 p}{\partial x_i \partial x_j} \tag{38}$$

This requires determination of the principal values and directions. Determination of the second derivatives of p^h needs future elaboration. Despite linear elements the curvatures of p^h should be interpolated and a second-order polynomial has to be adopted over a local patch of linear elements.

$$p^h = N\tilde{p} \tag{39}$$

Such a polynomial can be applied in a least square manner to fit the values at all nodal points within a patch of elements sharing a particular node. In problems where the gradient of a function may be preferred to the curvature, the maximum value of the gradient of *p*, for instance, can be easily determined at any point of the patch and in particular at the nodal points.

4.2 Mesh data transfer

A simplified data transfer procedure is obtained by nodal interpolation. The initial solution at the current mesh is interpolated from the solution of the previous mesh at the last time-step.

$$p_j(x,t) = \sum_{i=1}^{3} N_i(x) p_i(t) \tag{40}$$

where $p_j(x,t)$ is considered to be a vector of nodal values. For each node in the current mesh, the solution is interpolated locally from the element in the previous mesh containing the current node. To identify the element containing each specified node location efficient searching algorithms should be used.

5 Adaptive algorithms for FSI analysis

Eq. (7) could be rewritten as:

$$\nabla^2 p = \frac{1}{c_f}\ddot{p}; \quad p = f(x_1, x_2) \tag{41}$$

The second derivatives could be depicted in a tensor type notation as:

$$p_{ij} = \left(\frac{\partial^2 p}{\partial x_i \partial x_j} \right) \quad i,j = 1,2 \tag{42}$$

Principal values and directions of the second derivative tensor can be calculated from:

$$\det\begin{vmatrix} p_{11}-\lambda & p_{12} \\ p_{21} & p_{22}-\lambda \end{vmatrix}=0 \tag{43}$$

With the following two solutions, λ_1 (the minimum) and λ_2 (the maximum) values:

$$\lambda_1=\left|\frac{\mathrm{d}^2p}{\mathrm{d}X_1^2}\right|,\quad \lambda_2=\left|\frac{\mathrm{d}^2p}{\mathrm{d}X_2^2}\right| \tag{44}$$

where X_1 and X_2 are the directions of the minimum and maximum principal values. For a uniform distribution of the interpolation error:

$$h_{\min}^2\left|\frac{\mathrm{d}^2p}{\mathrm{d}X_2^2}\right|=h_{\max}^2\left|\frac{\mathrm{d}^2p}{\mathrm{d}X_1^2}\right|=\delta_{\min}^2\lambda_{\max} \tag{45}$$

$$\lambda_{\max}=\max\left(\left|\frac{\mathrm{d}^2p}{\mathrm{d}X_2^2}\right|_i\right)\quad \text{for all nodes } i \tag{46}$$

The user sets the limits of minimum and maximum element sizes as $\delta_{\min}$ and $\delta_{\max}$. Therefore, actual values of $h'_{\min}$ and $h'_{\max}$ at each node can be represented as:

$$h'_{\min}=\min\left(\delta_{\min},h_{\min}\right) \tag{47}$$

$$h'_{\max}=\min\left(\delta_{\max},h_{\max}\right) \tag{48}$$

Fig. 2 illustrates the FSI staggered solution. In each several time steps, the fluid domain solution results are transformed into the adaptive algorithm process as of Fig. 3. After error estimation and re-meshing, the new mesh is applied to the FSI algorithm for the next time step.

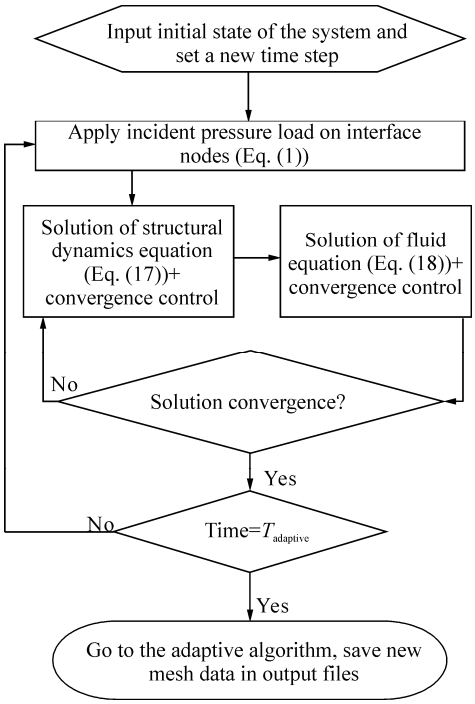

Fig. 2 Staggered FSI algorithm

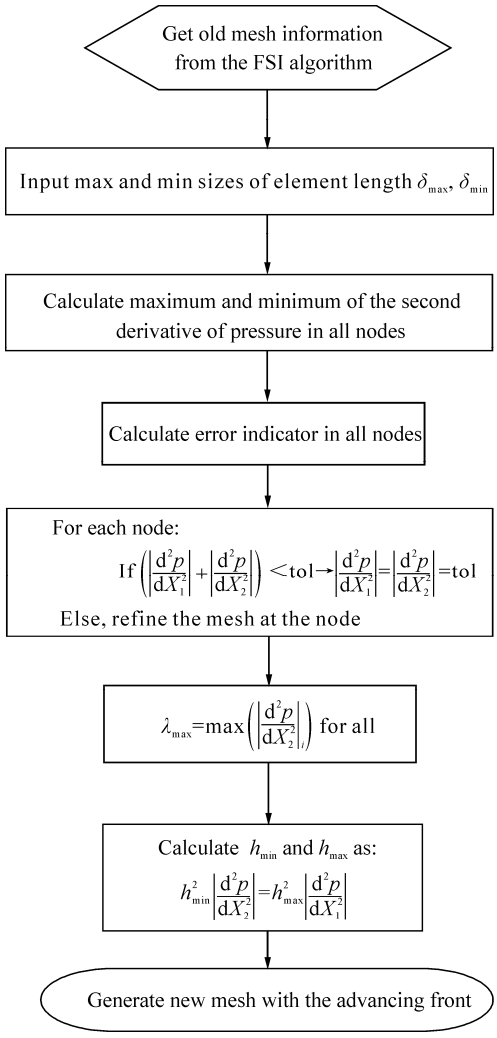

Fig. 3 Curvature based adaptive mesh generation algorithm

Error factors.

To evaluate the performance of transient-response histories with respect to a benchmark solution, a form of comprehensive error factor (C-error) given by Sprague and Geers (2006) is adopted:

$$C=\sqrt{V^2+P^2} \tag{49}$$

in which

$$V=\sqrt{\frac{V_{cc}}{V_{bb}}}-1 \tag{50}$$

$$P=\frac{1}{\pi}\arccos\left(\frac{V_{bc}}{\sqrt{V_{bb}V_{cc}}}\right) \tag{51}$$

where

$$V_{bb}=\frac{1}{(t_2-t_1)}\int_{t_1}^{t_2}b^2(t)\,\mathrm{d}t \tag{52}$$

$$V_{cc}=\frac{1}{(t_2-t_1)}\int_{t_1}^{t_2}c^2(t)\,\mathrm{d}t \tag{53}$$

$$V_{bc}=\frac{1}{(t_2-t_1)}\int_{t_1}^{t_2}b(t)c(t)\mathrm{d}t \tag{54}$$

In these equations, $c(t)$ is a candidate solution in the form of a response history, $b(t)$ is the corresponding benchmark history, and $t_1\le t\le t_2$ is the time span of interest. V is the magnitude error factor, which is insensitive to phase discrepancies, and P is the phase error factor, which is insensitive to magnitude discrepancies.

Sprague and Geers (2006) set $C<0.1$, $0.1\le C\le 0.2$ and $C>0.2$ as the bounds for satisfactory, marginal, and unacceptable error, respectively. These bounds can be used to decide $\Delta T_{\text{adaptive}}$ the maximum time period for mesh modification in specific problem where a reference solution is available otherwise a general empirical equation must be defined for determination of $\Delta T_{\text{adaptive}}$. In this study a fine mesh is used as the reference solution. If the C-error at the end of total time exceeds the maximum acceptable value, a reduction in $\Delta T_{\text{adaptive}}$ is needed. The following guideline is proposed for the maximum time period for mesh modification, $\Delta T_{\text{adaptive}}$ in a dynamic adaptive analysis.

$$\Delta T_{\text{adaptive}}\le 6\left(\frac{L_{\max}}{c_f}\right) \tag{55}$$

where

$$L_{\max}<\frac{c_f}{n_{\min}.f_{\max}} \tag{56}$$

In our experience for the maximum element size, six linear elements are considered to span the minimum wave length. According to Eq. (51), $\Delta T_{\text{adaptive}}$ is the time that is required by wave front to span maximum mesh size L_{mas}.

6 Results and discussion

Numerical examples of scatter wave propagation by adaptive finite elements are presented. Accuracy of the results using fine, equivalent and adaptive meshes is studied. The number of degrees of freedom (DOFs) in an equivalent mesh is approximately equal to the average number of DOFs in the adaptive meshes during the total analysis time. The latter procedure has been employed to assess the efficiency of the adaptive mesh.

6.1 Concrete wall under a triangular pulse

A concrete wall in contact with a semi-infinite reservoir is affected by a pulse of triangular plane wave. The results of adaptive and equivalent meshes are compared against that of a uniform fine mesh (as the reference solution). Fig. 4 shows the concrete wall with 0.3 m thickness and 2 m height.

Concrete material properties consist of mass density of 2400 kg/m^3, modulus of elasticity of 21.0 MPa and Poisson's ratio of 0.2. The incident pulse has amplitude of 1.0 MPa and a duration of 1.0 millisecond as defined in Fig. 5.

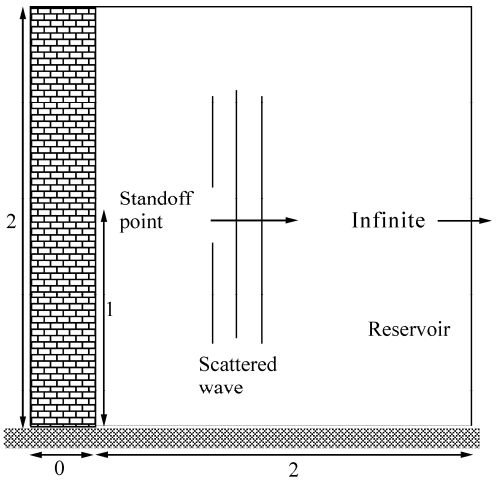

Fig. 4 Concrete wall under a triangular pulse

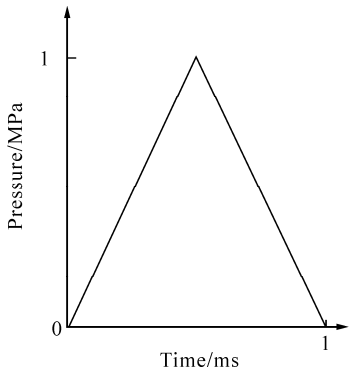

Fig. 5 Pressure loading at the stand-off point

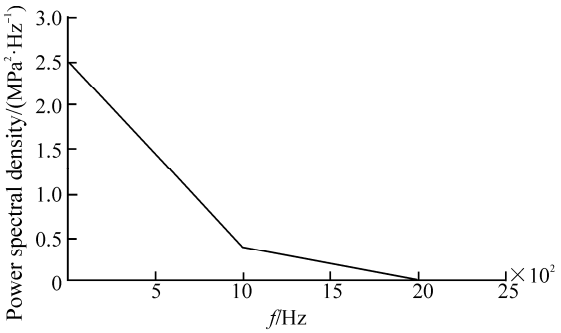

Fig. 6 Power spectral density of triangular loading

An incident plane pulse wave is considered inside the reservoir to represent a wave travelling toward the standoff point in the middle height of the wall. A non-reflective boundary condition is considered at just 2 m away from the wall in order to model the infinite boundary. The power spectral density of pressure incident wave has been plotted in Fig. 6 and the frequency content is determined.

$$L_{\max}<\frac{c_f}{n_{\min}f_{\max}}=\frac{1440}{6\times 2000}=0.12\,\text{m} \tag{57}$$

Accordingly, the maximum element size is 12 cm for the wave front but it could be increased elsewhere.

Generally, by medium frequencies (MF) one could refer to the range of 300 kHz to 3 000 kHz. Frequencies below and higher than this range could be denoted as low (LF), and high

(HF) frequencies, respectively. According to Fig. 6, the present problem can be categorized as an LF problem. The initial mesh shown in Fig. 7(a)–(c) and Fig. 7(d) is fairly fine. In Table 1, the number of nodes and elements in adaptive steps has been shown.

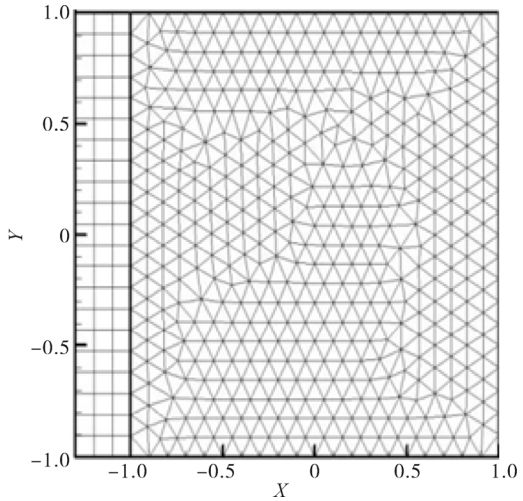

(a) T=0–0.5 ms (Initial uniform mesh)

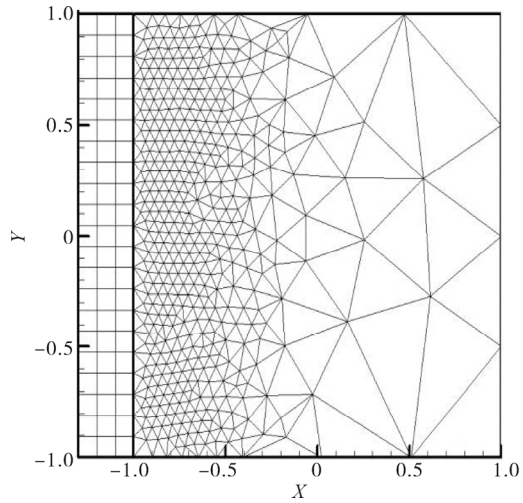

(b) T=0.5–1 ms

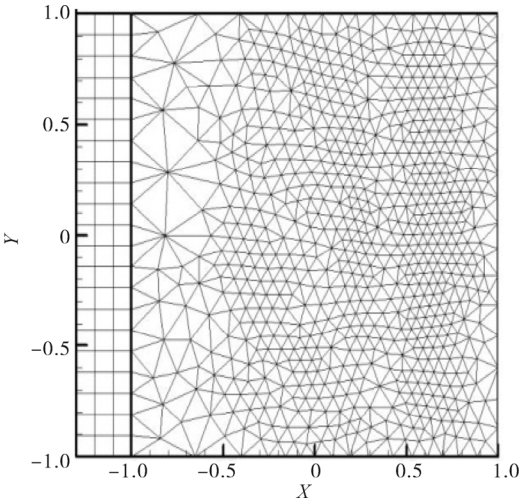

(c) T=1–1.5 ms

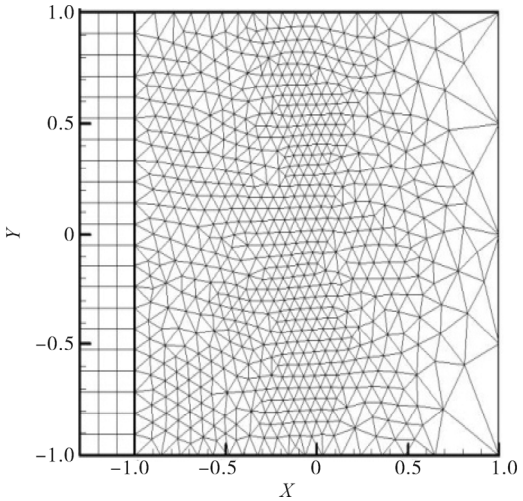

(d) T=1.5–2 ms (Final mesh)

Fig. 7 Successive updated meshes

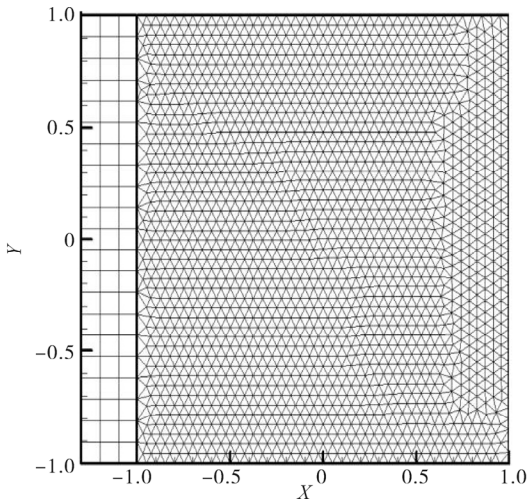

Fig. 8 Fine mesh with 1 877 nodes

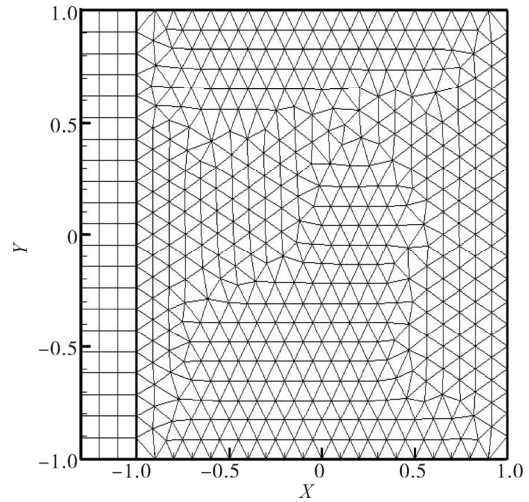

Fig. 9 Equivalent mesh with 609 nodes

For the initial and reference uniform fine meshes as shown in Fig. 8, the maximum size of the elements is considered as 10 cm. In this case the fluid and structure interface nodes are

kept coincident. The equivalent mesh is shown in Fig. 9. The total time required the scattered wave to travel from the wall to the infinite boundary is about 1.4 ms, after this time, the wave front exits the fluid domain and the pressure magnitude is decayed. According to Eq. (51), this period is divided into four 0.5 ms time steps and adaptation is performed once in each division

$$T_{\text{adaptive}} = 6\left(\frac{0.12}{1440}\right) = 0.5\,\text{ms} \tag{58}$$

In Figs. 10 to 12, adaptive steps are shown for the fluid domain.

When the wave front is near the wall (Fig. 10), pressure is an element is justified. A coarse mesh has been generated near the infinite boundary at x=2, while a fine mesh is necessary around the wave front, as shown in Fig. 11.

As the wave front is transmitted towards the infinite boundary, refinement is concentrated near this boundary. In Fig. 12 in the region near the wall a coarse mesh can be sufficient that has a non-essential limitation of at least one fluid element being attached to each structural element. Fig. 13 depicts the time history of the scattered pressure for a middle point of reservoir. The existing jumps in the "adaptive" curve are due to the particular interpolation scheme for the solution data transfer from the old to the new mesh. Table 2 compares the global C-error factor and the CPU time evaluated for different meshes. The pressure error norm is improved at about 18 percent compared to that of the equivalent mesh. The adaptive mesh CPU time also includes the mesh updating time. This result showed improvements in both precision and CPU time when using the adaptive mesh algorithm. Figs. 14 and 15 clearly showed that the overall response of the wall is improved when using the moving adaptive mesh rather than the equivalent uniform mesh.

Table 1 The number of nodes and elements in different meshes

Time Intervals/ms	Number of nodes	Number of elements	Mesh type
0–0.5	485	887	Initial mesh
1–0.5	452	399	2nd mesh
1.5–1	732	602	3rd mesh
2–1.5	765	941	4th mesh
—	608	707	Adaptive (average)
0–2	609	1 129	Equivalent mesh
0–2	1 877	3 611	Fine(reference) mesh

Table 2 Comparison of error factors and CPU times

Mesh type	C-error (Eq. (39))	CPU time/s
Adaptive	0.020	50
Equivalent	0.024	58
Fine(exact)	0.000	80

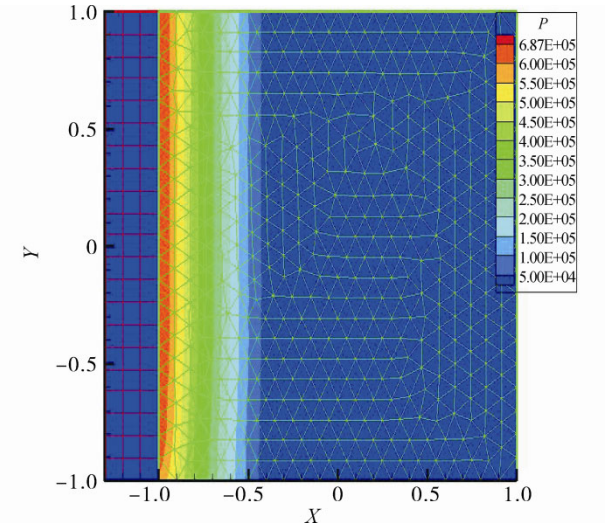

Fig. 10 Pressure contour at 0.5 ms

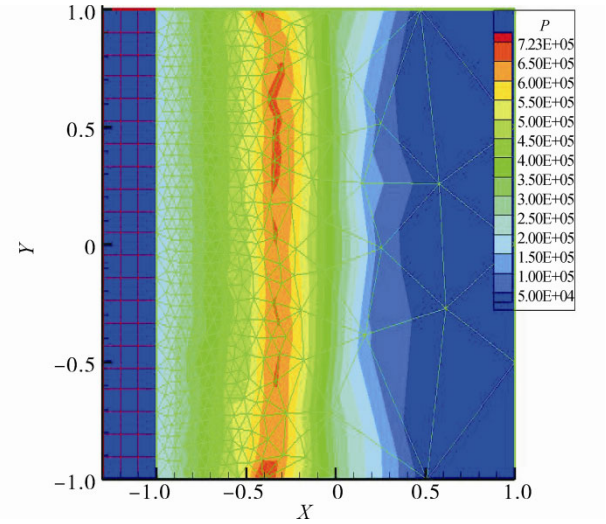

Fig. 11 Pressure contour at 1 ms

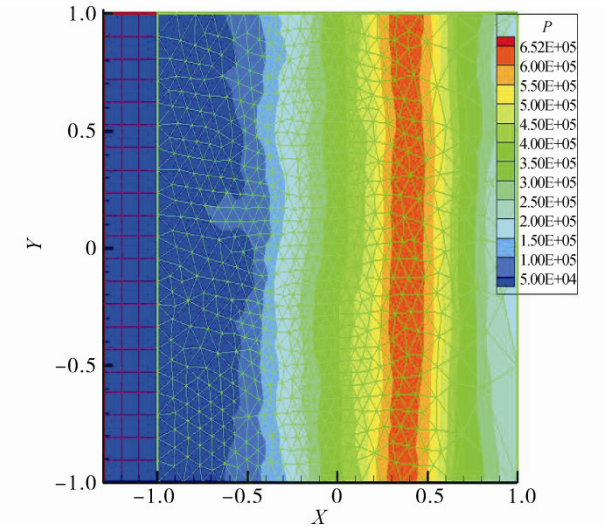

Fig. 12 Pressure contour at 1.5 ms

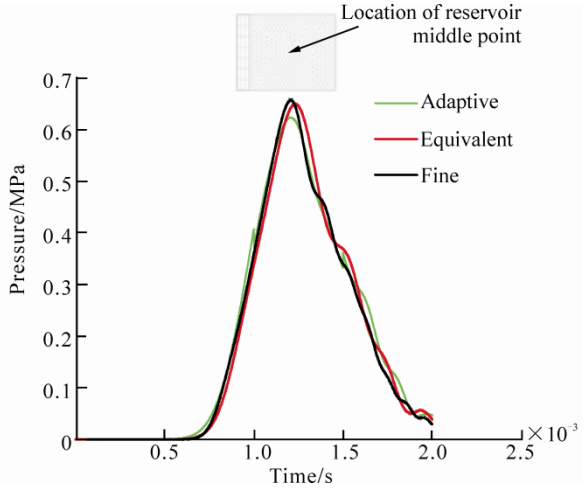

Fig. 13 Scattered pressure time history in the middle of reservoir

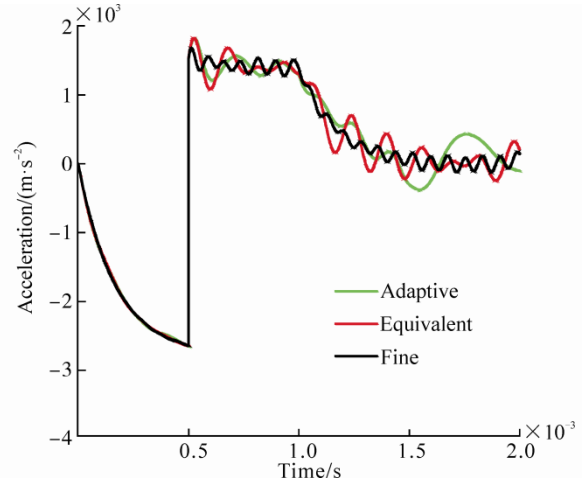

Fig. 14 Time history of acceleration in the *x* direction at the standoff point on the wall

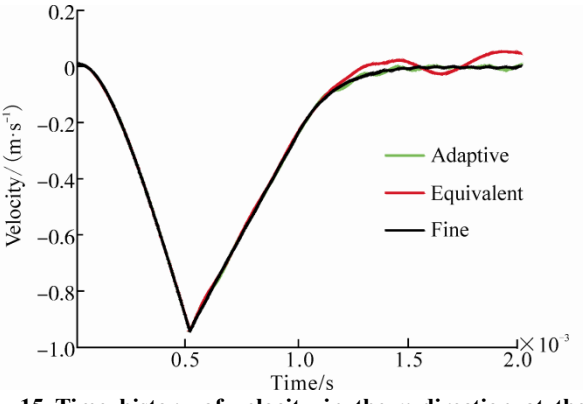

Fig. 15 Time history of velocity in the *x* direction at the standoff point on the wall

6.2 Concrete shell under step pulse

An infinite 0.15 m thickness concrete shell, in contact with a semi-infinite reservoir, is affected by a pulse of step plane wave, as depicted in Fig. 16.

The results of adaptive and equivalent meshes are compared with that of a uniform fine mesh. The incident pulse has amplitude of 1 MPa and a 1 μs rise time as shown in Fig. 17. The source of the pulse is at the center of the reservoir and the location of standoff is at the middle of the concrete shell. The power spectral density of pressure incident wave has been plotted in Fig. 18. The maximum element size is calculated as:

$$L_{\max} < \frac{C_f}{n_{\min} f_{\max}} = \left(\frac{1440}{6\times 500000}\right) = 0.00048\,\text{m} = 0.48\,\text{mm} \quad (59)$$

With this result it can be derived that a very fine mesh is required. However, for the sake of comparison of adaptive and equivalent meshes, some level of error with $f_{\max}$=2 000, which is related to 0.95 of maximum power spectral density is accepted. $L_{\max}$=10 cm and the initial mesh is generated according to Fig. 19.

Table 3 presents the mesh data in different adaptive analysis steps. The guideline in Eq. (51) proposes 0.41 s for the mesh updating time, with $L_{\max}$=10 cm, but for higher accuracy $\Delta T_{\text{adaptive}}$ is set 0.2 s. Figs. 19 and 20 show the initial and the equivalent meshes, respectively.

Table 3 Number of nodes and elements in different meshes

Time intervals/ms	Number of nodes	Number of elements	Mesh type
0–0.2	1 452	2 736	Initial mesh
0.4–0.2	145	229	2nd mesh
0.6–0.4	211	361	3rd mesh
0.8–0.6	262	463	4th mesh
1–0.8	213	365	5th mesh
1–1.2	265	465	6th mesh
1–1.2	229	394	7th mesh
1.2–1.4	399	716	Adaptive (average)
0–1.4	390	679	Equivalent mesh
0–1.4	1 452	2 736	Fine mesh

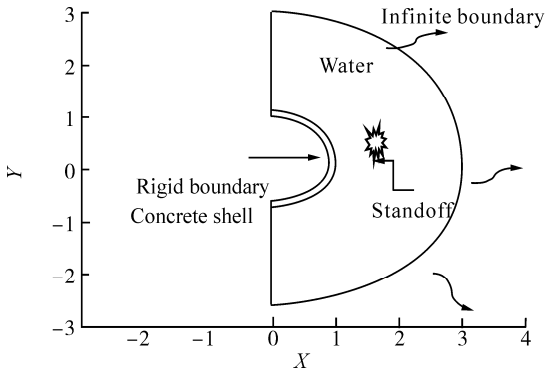

Fig. 16 Plane strain concrete shell under step pulse

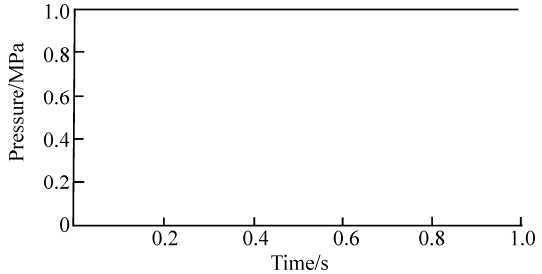

Fig. 17 Pressure loading at the standoff point (rise time=1 μs)

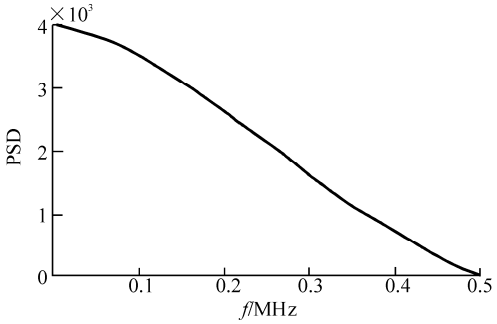

Fig. 18 Power spectral density of step loading

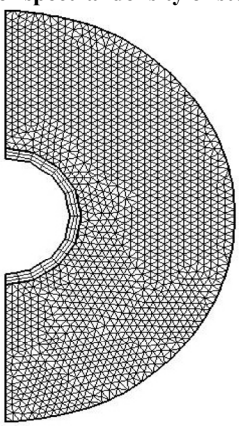

Fig. 19 Initial mesh with 1 452 nodes

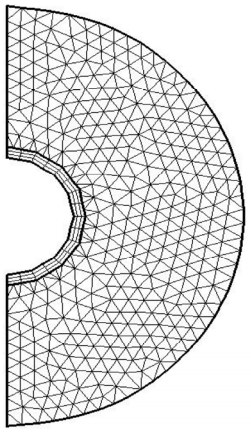

Fig. 20 Equivalent mesh with 399 nodes

Fig. 21 shows successive updated meshes based on the curvature indicator criterion. When the scattered wave front propagates almost in radial direction, the fine part of the mesh moves with it until it reaches to the infinite boundary. Since L_{max} is very small and a relatively large element size is still used for the fine mesh, oscillations are expectedly observed even in the fine mesh. This is illustrated in Fig. 22. The effect of these oscillations is not considered in the present comparison of adaptive and equivalent meshes.

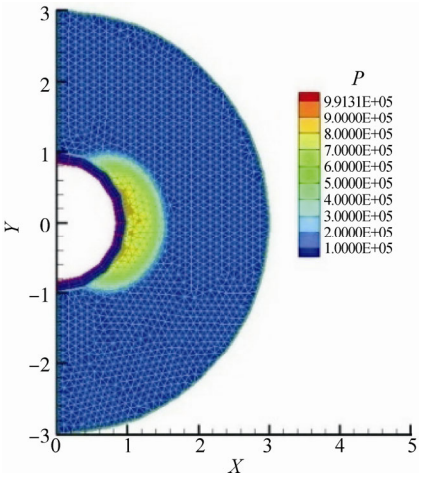

(a) T= 0.2 ms (Initial uniform mesh)

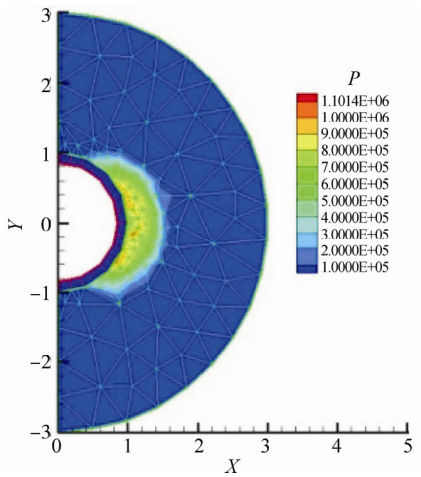

(b) T=0.4 ms

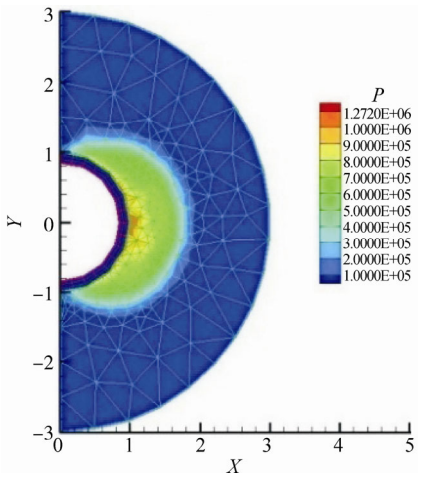

(c) T=0.6 ms

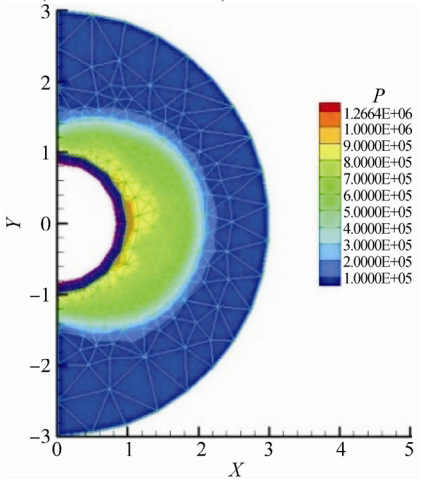

(d) T=0.8 ms

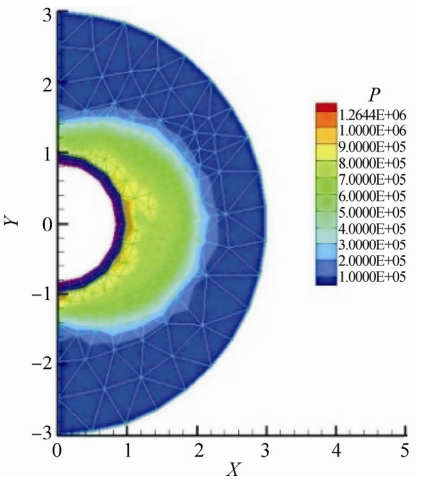

(e) T=1 ms

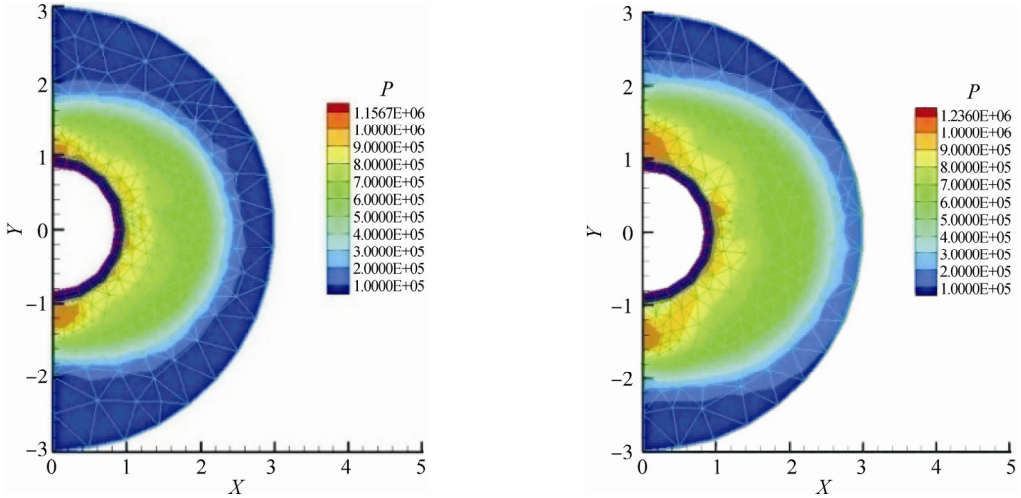

(f) T=1.2 ms (g) T=1.4 ms (Final mesh)

Fig. 21 Successive updated meshes and pressure

According to Table 4 the pressure C-error factor of adaptive mesh is 11 percent less than that of the equivalent mesh. Also, CPU time has been reduced when using adaptive mesh. By comparing Table 2 and Table 4 it can be seen that the adaptive mesh is more effective for higher frequency contents of the incident wave loading.

The time histories of acceleration and velocity are plotted in Figs. 23 and 24.

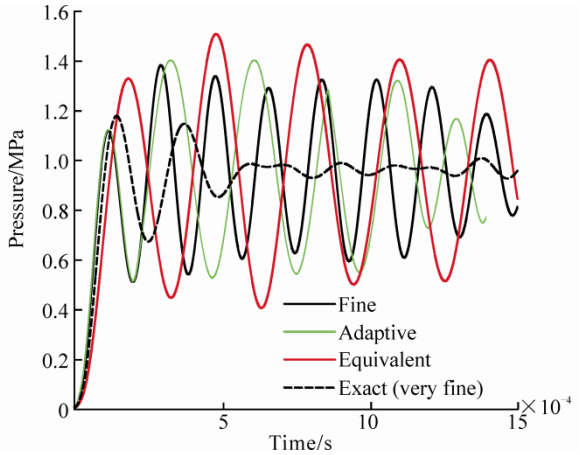

Fig. 22 Time history of pressure at the standoff point

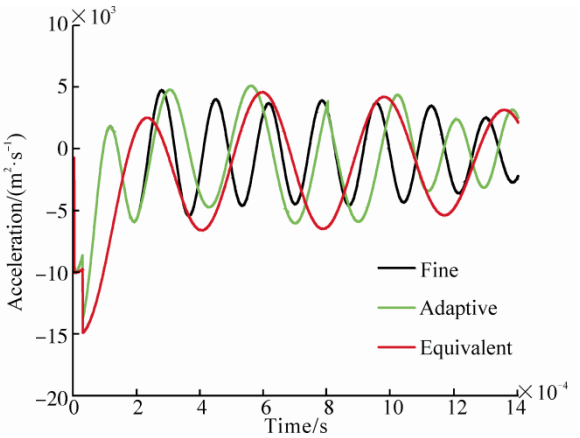

Fig. 23 Time history of acceleration in x direction at the standoff point on the wall

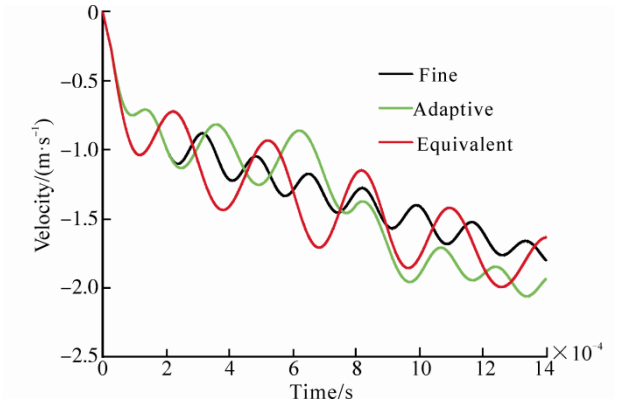

Fig. 24 Time history of velocity in x direction at the standoff point on the wall

Adaptive and equivalent C-error factors are also compared with that of the fine mesh in Table 5. This showed that the velocity error factor of the adaptive mesh is 12.5 percent less than that of the equivalent mesh. This is an indication of the efficiency of dynamic adaptive solution.

Table 4 Comparison of error factors and CPU times

Mesh type	C-error (Eq. (3))	CPU time/s
Adaptive	0.163 0	30
Equivalent	0.17	48
Very fine (4326 Nodes)	0.00	214

Table 5 Comparison of horizontal velocity error norms

Mesh type	C-error (Eq. (39))
Adaptive	0.063
Equivalent	0.072
Fine	0.000

7 Conclusions

This paper has presented a dynamic adaptive finite element analysis strategy for acoustic wave propagation due to

underwater explosion in fluid-structure interaction problems. This approach is based on the C-error factor, which has an appropriate adaptive mesh refinement that is carried out at certain time intervals during the total time of wave propagation. It has been numerically illustrated that the error indicator based on the curvature could produce improvement as high as 22 percent in C-error factor for the pressure time history for the test cases considered. Similar results have been obtained for the response of velocity and acceleration. The curvature error indicator can be an effective tool for examining the adequacy of a finite element meshes by identifying the regions where mesh refinement is necessary in acoustic adaptive dynamic analysis. The proposed guideline for the mesh updating time interval can be used in the dynamic adaptively process and its performance may be investigated in future studies. The same procedure can be used with gradient based formulation for very low frequency waves. Therefore, reduction in computational cost and increase in accuracy for high frequency wave is the obvious improvement compared to other traditional works.

References

Bausys R, Wiberg NE (1999). Adaptive finite element strategy for acoustic problems. *Journal of Sound and Vibration*, **226**(5), 905-922.
DOI: 10.1006/jsvi.1999.2323

Bell J, Berger M, Saltzman J, Welcome M (1994). Three dimensional adaptive mesh refinement for hyperbolic conservation laws. *SIAM Journal on Scientific Computing*, **15**(1) 127-138.
DOI: 10.1137/0915008

Berrone S, Marro M (2009). Space-time adaptive simulations for unsteady Navier-Stokes problems. *Computers & Fluids*, **38**(6), 1132-1144.
DOI: 10.1016/j.compfluid.2008.11.004

Bouillard Ph, Allard JF, Warzee G (1996). Superconvergent patch recovery technique for the finite element method in acoustics. *Communications in Numerical Methods in Engineering*, **12**(9), 581-594.
DOI: 10.1002/(SICI)1099-0887(199609)12:93.3.CO;2-J

Cole RH (1948). *Underwater explosions*. Princeton University Press, Princeton, USA.

Dapogny C, Dobrzynshi C, Frey P (2014). Three-dimensional adaptive domain remeshing, implicit domain meshing, and applications to free and moving boundary problems. *Journal of Computational Physics*, **262**(4), 358-378.
DOI: 10.1016/j.jcp.2014.01.005

Emamzadeh S. Sh (2008). *An adaptive finite element analysis of acoustic waves propagation due to underwater explosion for fluid-structure interaction problems*. PhD thesis, Tarbiat Modares University, Tehran, 62-66. (in Persian)

Ghanaat Y, Clough W, Redpath BB (1992). Experimental study of dam-water-foundation interaction. *Proceedings of the Tenth World Conference on Earthquake Engineering*, Madrid, Spain, 19-24.

Gilardo FX (1995). *A space marching adaptive re-meshing technique applied to the 3D Euler equations for supersonic flow*. PhD thesis, University of Virginia, Charlottesville, 59-80.

Harari I, Grosh K, Hughes TJR, Malhotra M, Pinnsky PM, Stewart JR, Thompson LL (1996). Recent development in finite element methods for structural acoustics. *Archives of Computational Methods in Engineering*, **3**(2-3), 131-311.
DOI: 10.1007/BF03041209

Hua F, Wang P, Chen X, Feng H (2015). An adaptive mesh method for 1D hyperbolic conservation laws. *Applied Numerical Mathematic*, **91**, 11-25.
DOI: 10.1016/j.apnum.2014.10.008

Kadioglu SY, Sussman M (2008). Adaptive solution techniques for simulating underwater explosions and implosions. *Journal of Computational Physics*, **227**(3), 2083-2104.
DOI: 10.1016/j.jcp.2007.10.019

Kim JH, Shin HC (2008). Application of the ALE technique for underwater explosion analysis of a submarine liquefied oxygen tank. *Ocean Engineering*, **35**(8-9), 812-822.
DOI: 10.1016/j.oceaneng.2008.01.019

Howell LH, Bell J (1997). An adaptive-mesh projection method for viscous incompressible flow. *SIAM Journal on Scientific Computing*, 18(4), 996-1013.
DOI: 10.1137/S1064827594270555

Mair HU (1999). Review: Hydrocodes for structural response to underwater explosions. *Shock and Vibration*, **6**(2), 81-96.
DOI: 10.1155/1999/587105

Pember RB, Howell LH, Bell J, Colella P, Crutchfield WY, Fiveland WA, Jessee JP (1998). An adaptive projection method for unsteady low-Mach number combustion. *Combustion Science and Technology*, **140**(1-6), 123-168.
DOI: 10.1080/00102209808915770

Peraire J, Vahdati M, Morgan K, Zienkiewicz OC (1987). Adaptive re-meshing for compressible flow computations. *Journal of Computational Physics*, **72**(2), 449-466.
DOI: 10.1016/0021-9991(87)90093-3

Ross MR, Felippa CA, Park KC, Sprague MA (2008). Treatment of acoustic fluid-structure interaction by localized Lagrange multipliers: Formulation. *Computer Methods in Applied Mechanics and Engineering*, **197**(33-40), 3057-3079.
DOI: 10.1016/j.cma.2008.02.017

Ross MR, Sprague MA, Felippa CA, Park KC (2009). Treatment of acoustic fluid–structure interaction by localized Lagrange multipliers and comparison to alternative interface-coupling methods. *Computer Methods in Applied Mechanics and Engineering*, **198**(9-12), 986-1005.
DOI: 10.1016/j.cma.2008.11.006

Shin YS (2004). Ship shock modeling and simulation for far-field underwater explosion. *Computers & Fluids*, **82**(23-26), 2211-2219.
DOI: 10.1016/j.compstruc.2004.03.075

Skamarock WC, Klemp JB (1993). Adaptive grid refinement for two-dimensional and three-dimensional non hydrostatic atmospheric flow. *Monthly Weather Review*, **121**(3), 788-804.

Sommerfeld A (1949). *Partial differential equations in physics*. Academic Press, New York, 188-190.

Sprague MA, Geers TL (2006). A spectral-element/finite-element analysis of a ship-like structure subjected to an underwater explosion. *Computer Methods in Applied Mechanics and Engineering*, **195**(17-18), 2149-2167.
DOI: 10.1016/j.cma.2005.03.007

Sprague MA, Geers TL (2008). Legendre spectral finite elements for structural dynamics analysis. *Communications in Numerical Methods in Engineering*, **24**(12), 1953-1965.
DOI: 10.1002/cnm.1086

Steinthorsson E, Modiano D, Crutchfield WY, Bell JB, Colella P (1995). An adaptive semi-implicit scheme for simulations of unsteady viscous compressible flow. *Proceedings of the 12th AIAA Computational Fluid Dynamics Conference*, Orlando, USA, AIAA Paper 95-1727-CP.

Stevens DE, Bretherton CS (1996). A forward-in-time advection scheme and adaptive multilevel flow solver for nearly incompressible atmospheric flow. *Journal of Computational Physics*, **129**(2), 284-295.
DOI: 10.1006/jcph.1996.0250

Tetambe RP, Rajakumar C (1996). Estimation of error in finite element acoustic analysis. *Computers and Structures*, **61**(1), 13-19.
DOI: 10.1016/0045-7949(96)00036-3

Wardlaw A (1998). *Underwater explosion test cases*. Office of Naval Research, Virginia, United States, Technical Report IHTR 2069, ADB238684.

Yu Tiantang (2009). Dynamical response simulation of concrete dam subjected to under water contact explosion load. *2009 World Congress on Computer Science and Information Engineering*, Los Angeles, USA, 767-774.
DOI: 10.1109/CSIE.2009.106

Zienkiewicz OC, Taylor RL, Nithiarasu P (2005). *The finite element method for fluid dynamics*. Sixth edition, Butterworth-Heinemann, Oxford, United Kingdom, 465-478.

2015 International Ocean Technology Conference & Expo (IOTCE 2015)

September 1-3, 2015, Qingdao, Shandong, China

The 2015 International Ocean Technology Conference & Expo (IOTCE 2015) will be held in the heart of the rapidly expanding Blue Economic Zone in Shandong Peninsula, Qingdao. It is a platform for the international and cooperative development of the national marine economy, in support of the offshore oil & gas, oceanographic, environmental and maritime industries around the world. IOTCE 2015 is a bridge for communication, and a showcase platform for engineers, scientists, and industry professionals to share and exchange ideas in their industries, and expand their network. IOTCE 2015 includes a state-of-the-art marine science & technology and equipment exhibition, and a large-scale international academic conference.

Marine Technology & Equipment Exhibition

The International Ocean Technology Conference & Expo is a state-of-the-art showcase of the latest advancements in the marine science & technology industries. It provides a unique opportunity to gather global marine science & technology advantages as well as exhibiting achievements of marine industry.

Exhibition agenda:

August 30-31: Exhibition Setup
September 1-3: Exhibition IOTCE Exhibition Area Division:

(1) Development Technology and Equipment for Ocean Oil, Gas, and Mineral Resources
(2) Marine Engineering Technology and Equipment, Harbor Machinery
(3) Technology and Equipment for Ocean Renewable Resource
(4) Underwater Technology and Equipment, Ocean Exploration and Detection Instruments

During the exhibition, venues are available for companies to host conferences to promote new products and new technology, hold commercial negotiation and cooperation sessions, and host press conferences.

International Academic Conference

The conference begins with the main introductory session and keynote speech. The introductory session demonstrates the future of the marine industry, including its challenges and direction. The remaining sessions cover topics ranging from offshore platform and technology design to underwater technology development.